Computation and numerical modeling of fuel concentration distribution and current density on performance of the microfluidic fuel cell

6 authors, including:

Yusuf Dewantoro Herlambang
Politeknik Negeri Semarang
69 PUBLICATIONS **110** CITATIONS

SEE PROFILE

Anis Roihatin
Politeknik Negeri Semarang
16 PUBLICATIONS **93** CITATIONS

SEE PROFILE

Kurnianingsih Kurnianingsih
Politeknik Negeri Semarang
44 PUBLICATIONS **346** CITATIONS

SEE PROFILE

Totok Prasetyo
Politeknik Negeri Semarang
29 PUBLICATIONS **89** CITATIONS

SEE PROFILE

Computation and numerical modeling of fuel concentration distribution and current density on performance of the microfluidic fuel cell

Yusuf Dewantoro Herlambang, Anis Roihatin, Kurnianingsih, Totok Prasetyo, Shun-Ching Lee, and Jin-Cherng Shyu

View Online   Export Citation

ARTICLES YOU MAY BE INTERESTED IN

Computation and Numerical Modeling of Fuel Concentration Distribution and Current Density on Performance of The Microfluidic Fuel Cell

Yusuf Dewantoro Herlambang[1, a)], Anis Roihatin[1], Kurnianingsih[2, b)], Totok Prasetyo[1], Shun-Ching Lee[3] and Jin-Cherng Shyu[3]

[1]*Department of Mechanical Engineering, Politeknik Negeri Semarang*
Jl. Prof. Sudarto, SH Temabalang Semarang 50275, Indonesia
[2]*Department of Electrical Engineering, Politeknik Negeri Semarang*
Jl. Prof. Sudarto, SH Temabalang Semarang 50275, Indonesia
[3]*Department of Mechanical Engineering, National Kaohsiung University of Science and Technology*
415 Jiangong Rd, Sanmin Dist., Kaohsiung 80778, Taiwan

[a)] Corresponding author: masyusufdh@polines.ac.id
[b)] kurnianingsih@polines.ac.id

Abstract. This study numerically investigates current density and fuel concentration on the performance of microfluidic fuel cells that breathe air as an oxidant. The microfluidic fuel cells having a microchannel width of 1.0 mm and 50 μm in-depth with an electrode spacing of 0.3 mm. The concentration formic acid of 0.3 M, 0.5 M, and 1.0 M mixed with 0.5 M sulfuric acid (supporting electrolyte) in aqueous solution was used as fuel and another inlet a stream of 0.5 M sulfuric acid as an electrolyte which were varied at an inlet flow rate of 0.3, 0.5, and 0.7 mL/min. First, a three-dimensional microfluidic fuel cell model was established using COMSOL Multiphysics 5.1 to simulate the fuel cell performance. Subsequently, both V-I curves obtained from simulation and published experimental data under similar operating condition were compared to assure the validity of the simulation. The transport phenomena in the microfluidic fuel cells were formulated with continuity equation, momentum equation, species transport equation, and charge equation. The porous media flow in the gas diffusion layer was described by Brinkman equation. The Butler-Volmer equations were applied to get the V-I curves. The maximum power density of the fuel cell at 0.7 mL/min fed with 0.3 M, 0.5 M, and 1.0 M formic acid for the measured was approximately 27 mW/cm^2, 30 mW/cm^2, and 36 mW/cm^2, respectively, while for the simulation was approximately 21.64, 29.82, and 36.57 mW/cm^2, respectively.

Keywords: air-breathing; microfluidic, fuel cells; formic acid; fuel utilization

INTRODUCTION

The development of novel miniaturized fuel cell based on MEMS (micro electro mechanical systems) are considered as promising candidate of alternative power sources for future generation due to its potentially wide range applications in portable devices [1-5], such as cell phones, laptop, clinical diagnostics, small stationary power etc. Microfluidic cells have some significant intrinsic advantages than conventional Li-battery [6-8], i.e. fuel cell ability to continuously generate power as long as both fuel and oxidant are supplied into the cell, higher energy density, longer lifetimes without replaced and recharged periodically, more reliable related in diverse power input, no emissions and no pollutions, and no interrupts if integrated into the system. Power sources are corresponding for fuel cell applications is batteries in which the use of a longer operating time without needed frequent recharging power.

Conversely, the batteries have a shorter operating time span which needed recharging again and is determined by the dimension of the battery as energy storage.

Over the past decade, advancement in miniaturization technology of fuel cell which it related to fuel cell architectures have been studied many researchers [9-14]. Microfluidic fuel cell architectures can be classified into eight major types: (i) fluidic phases of the fuel and oxidant streams are gaseous fuel and oxidant, liquid fuel and gaseous oxidant, liquid fuel and oxidant; (ii) fuel types are hydrogen, methanol, formic acid, vanadium ions including V^{2+}/vanadium (II) and V^{3+}/vanadium (III); (iii) oxidant types are oxygen, hydrogen peroxide, and VO_2^+/vanadium (IV) oxide and VO^{2+}/vanadium (V) oxide; (iv) channel configurations are I, H, Y, F, T-channel; (v) electrode materials are Pt/Ru platinum-rutherium, Pt/Pd platinum-palladium, Pd/C palladium-carbon; (vi) flow types are flow-through anode porous electrode, flow-over anode porous electrode, radial porous electrode, air-breathing cathode for oxygen; (vii) porous electrode positions/configuration are bottom wall, side wall, bottom and top walls, side-top-and bottom walls, and, both electrodes at under channel; (viii) fuel-oxidant flow direction are horizontal-vertical, and fuel flow between solid-free standing electrode in a hexagonal pattern. The configuration of the microfluidic fuel cells is classified into three generations [14, 25]. The first generation MFCs-G1 is Y-shape MFCs, the aqueous fuel stream at anode channel inlet and an oxidant stream at the cathode channel inlet flows in parallel along with microchannel, while the anode and cathode electrode on the opposite side of the walls. In the second generation MFCs-G2, two streams fuel and oxidant are incorporated in parallel horizontally flowing side by side in Y or T-shape microchannel which anode and cathode porous electrodes placed on the bottom side of the microchannel. The third generation MFCs-G3, same with the second generation employed T or Y-shape microchannel, but there was air-breathing on the cathode electrode inlet used to flowing the oxidant. The aqueous fuel stream at the anode inlet and the electrolyte stream employed at the cathode inlet which called as air-breathing membraneless fuel cells (AMFCs). The air-breathing membraneless fuel cells can be classified into two types of working operation which are the active AMFCs and passive AMFCs, respectively. The active AMFCs is air-breathing membraneless fuel cells with the fuel reservoir which the air flowing into the microchannel with controlled pressure on the reservoir inlet side. For the passive AMFCs, the inlet cathode electrode on the lower side (holes) is employed for oxygen as the oxidant flows from the air supply around.

Applications for off-grid power generation as a power source for portable devices must have design features low power, but high energy density and operating at low temperatures. A novelty design and structure of microfluidic fuel cells was proposed by Jayashree et al. [15] in 2005, also known as membraneless micro fuel cells (MFCs) or laminar flow-based fuel cells (LFFCs). Membrane-less microfluidic fuel cells (MFCs) is a miniaturized fuel cell without needing a proton membrane. They use an electrolyte as a substitute of the membrane which used to exchange proton. Microfluidic fuel cells contain liquid fuel and oxidant that flowing side by side along the microchannel [17-19]. Microfluidic fuel cells utilize the drawback of diffusive and convective mixing fluid by applying laminar flow at low Reynold number separate the fuel and oxidant [20, 21], also to eliminate polymer membrane used in traditional fuel cells. Fluid flows either flowing through, flowing over, flowing between a top and down along the anode and cathode electrode. In the channel cell and porous media, mixing of the species can be occurred only in the diffusion process. The performance by enhancing an efficiency of current air-breathing microfluidic fuel cells have been investigated [27-30]. Therefore, the aims of this study are to investigate various effects on the performance of direct formic acid microfluidic fuel cells that breathe air as an oxidant. Three-dimensional numerical simulation is developed for a formic acid air-breathing microfluidic fuel cells with flow-over anode-cathode electrode. The present computational model simulation is validated towards the experimental study and others published data.

NUMERICAL METHOD

Computational Domain

In Fig. 1 schematically illustrates the computation domain and geometry a miniaturized fuel cell T-shaped air-breathing DFAFC (Direct Formic Acid Fuel Cells). The air-breathing direct formic acid microfluidic fuel cell having a 1.5-mm-wide and 0.05-mm-deep T-shape microchannel were numerically investigated at volumetric flow rates ranging from 0.05 mL/min to 0.5 mL/min. The spacing between two 20- mm-long, 0.6-mm-wide and 900-μm-thick GDEs in a fuel cell was 0.3 mm. The mixture of formic acid and 0.5-M H_2SO_4 was used as the fuel, while a 0.5-M H_2SO_4 stream was used as liquid electrolyte. The concentration of formic acid was 0.3 M, 0.5 M and 1.0 M.
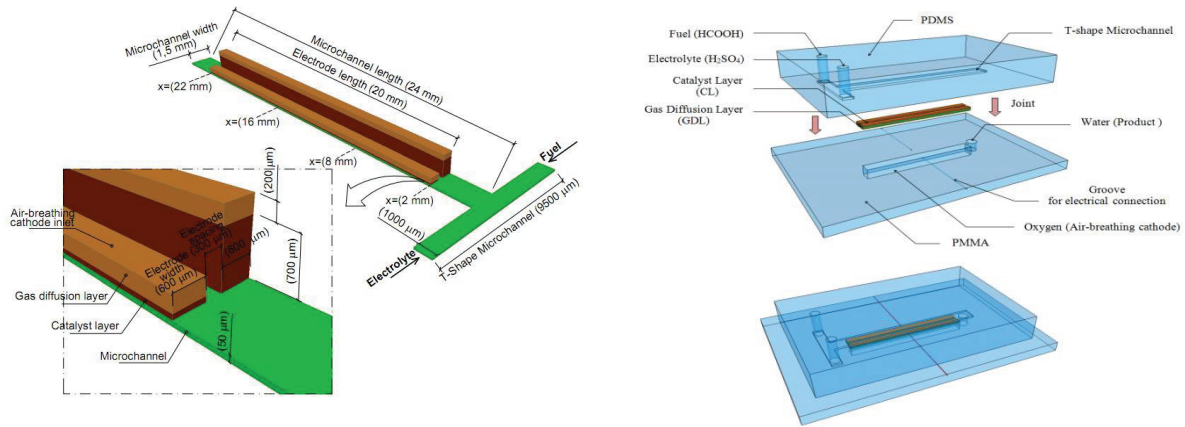
FIGURE 1. Schematic of the structural model T-shaped air-breathing direct formic acid fuel cells used in numerical simulation and the experimental study

Experimental Methods

The model formed by five layers that are composed of a microchannel, anode catalyst layer, anode gas diffusion layer, cathode catalyst layer, cathode gas diffusion layer. In detail, the microchannel having two inlets, both anode inlet as fuel (formic acid mixed with sulfuric acid) and cathode inlet are filled with sulfuric acid as a proton conductor. In such systems for the fluid delivery, both formic acid (1 M) as a fuel solution mixing sulfuric acid (0.5 M) at anode channel side and as an electrolyte used sulfuric acid (0.5 M) place take on the cathode channel side are injected together into the end of the channel outlet by two syringe pumps.
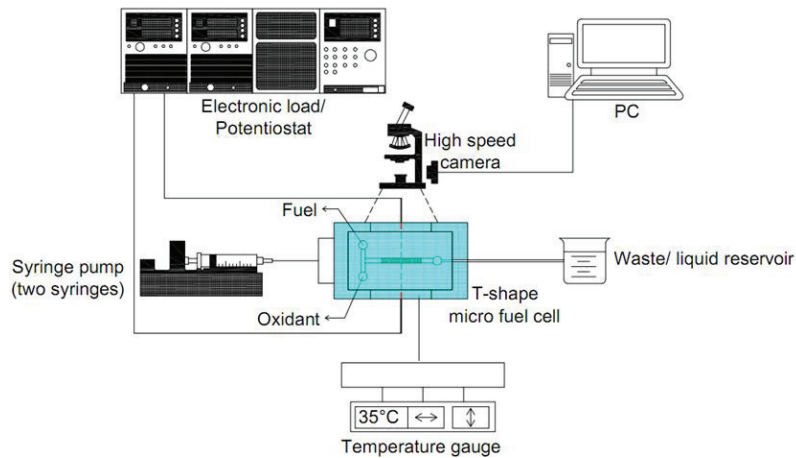

FIGURE 2. Schematic of the experiment set-up

While sufficiency of the oxygen supply from the air is chosen as an oxidant. The electrolyte solution was added to both anode and cathode electrolyte channel to serve sufficiency proton ions, also the better proton conductivity at the electrochemical kinetic reactions. The anode and cathode porous electrode are deposited on the bottom side of a microchannel. In both the anolyte (fuel solution) and catholyte (electrolyte solution) stream takes place to contact and a reaction of the species so that proton ions produced at the anode side can transfer from the anolyte to the cathode electrode. In the air-breathing system, a stream of oxygen is exposed to the ambient air supply as well as the oxidant, and from cathode GDL bottom side penetrates into the porous electrode in contact with the electrolyte solution to generate water at the end of the channel outlet. The bottom surfaces of the anode and cathode electrode are electric

ground and electric potential, respectively. They are as current collectors that generate an electronic conductivity connected to an electronic load circuit.

TABLE 1 Performance of direct formic acid fuel cell

Authors	Fuel/oxidant	Electrolyte	Current density (mA/cm^2)	Power density (mW/cm^2)	Channel size (mm)	Model features
Shaegh et al. [7]	HCOOH/air	H_2SO_4	7.92	7.9	W x H x L 2.0 x 0.9 x 50	Air-breathing MFCs with a porous planar anode
Shaegh et al. [8]	HCOOH/air	H_2SO_4	140	29	W x H x L 3.0 x 0.5 x 30	Air-breathing MFCs using fuel reservoir
Cohen et al. [23]	HCOOH/O$_2$ +H$_2$SO$_4$	H_2SO_4	0.88	0.085	W x H x L 5 x 0.25 x 50	Novel design for planar MFCs
Zhang et al. [5]	HCOOH/air	H_2SO_4	117.6	13.2	W x H x L 2.0 x 3.0 x 44	Air-breathing MFCs with flow-over and flow-through anodes
Xuan et al. [18]	HCOOH/air	H_2SO_4	300	58	W x H x L 0.75 x 0.2 x 20.5	2G of Air-breathing MFCs with flow-over anode
Khabbazi et al. [6]	HCOOH/O$_2$ +H$_2$SO$_4$	H_2SO_4	6	3.6	W x H x L 2.0 x 0.5 x 30	The effect of channel and electrode geometry
Jayashree et al. [14]	HCOOH/O$_2$ +H$_2$SO$_4$	H_2SO_4	165	55	W x H x L 10 x 5.9 x 50	1G and 2G of Performance MFCs with flow-through anode
Zhang et al. [16]	HCOOH/O$_2$ +H$_2$SO$_4$	not used	27	3.8	W x H x L 2.0 x 1.0 x 6.5	MFCs, improving fuel utilization and fuel concentration
Zhu et al. [2]	HCOOH (1M)/air	H_2SO_4	118.3	21.5	W x H x L 2.5 x 6.3 x 40	Air-breathing MFCs based on Cylinder electrodes
Choban et al. [24]	HCOOH/O$_2$ +H$_2$SO$_4$	not used	4	2.4	W x H x L 1.0 x 1.0 x 30	1G of MFCs based on laminar flow
Moreno et al. [22]	HCOOH/air	not used	152	27.3	W x H x L 1.0 x 0.3 x 20	3G of T-shape DFAFCs design and performance evolution
Ye et al. [26]	HCOOH/air	H_2SO_4	250	75	W x H x L 2.5 x 6.3 x 40	Air-breathing MFCs with an array of cylinder anodes
Zuria et al.	HCOOH/air	not used	152	27.3	W x H x L 1.0 x 0.3 x 20	3G of T-shape DFAFCs design and performance evolution
Shyu et al. [12]	HCOOH + H$_2$SO$_4$/air	H_2SO_4	120	36	W x H x L 1.5 x 0.05 x 30	3G of Y-shape air-breathing MFCs with flow over the electrode

The cell performance comparison of different microfluidic fuel cell architectures running on formic acid based on the electrode design and different operating conditions is reviewed in Table 1. In these table shows that the value of the current density of the cell ranges from 6 mA/cm^2 to 300 mA/cm^2, while for the magnitude of the power density from 0.085 mW/cm^2 to 75 mW/cm^2.

In the present study, a fundamental roadmap is used to explain a general overview about modeling the transport and electrochemical phenomena on the performance of a microfluidic fuel cell, Fig. 3.
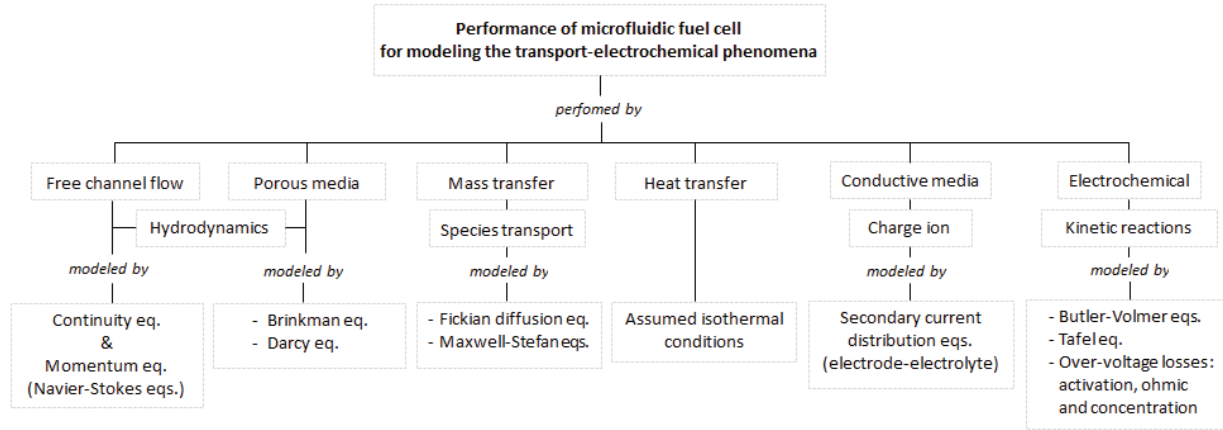
FIGURE 3. Fundamental roadmap of the microfluidic fuel cell

In this study, the numerical simulation of the microfluidic fuel cells performed with computation domain as shown in Fig. 1 was based on a 3-dimensional model implemented by commercially available software COMSOL Multiphysics 5.1. The three dimensional numerical simulation model was performed based on the following assumptions:

1. Fuel cell system is three-dimensional, steady-state and isothermal domain;
2. Laminar flow, incompressible fluid flow, continuity at all internal boundaries and body forces are negligible;
3. The physical properties of the electrodes (catalyst layers and GDLs) are considered as an isotropic porous media and homogeneous;
4. The solutions are dilute;
5. Proton transport from anode to cathode is by electro-migration only.
6. Oxygen transport in the porous air-breathing cathode is by diffusion only;
7. Product carbon dioxide is fully dissolved in the solution;
8. The porous media flow in the gas diffusion layer was described by Brinkman equation;
9. Electrochemical reaction take place at 300 K, 1 atm which is governed by Butler-Volmer electrode kinetics to get the *V-I* and *P-I* curves.

Governing equations

In order to predict the effect polarization behaviors of the transport phenomena on fuel cell performance, the governing equations are performed based on partial differential equations in 3-dimensional Cartesian coordinates in the model. A set of steady-state conservation equation is used to govern the computation domain of the performance of model fuel cell which were formulated with continuity equation and momentum equation, species transport equation, and charge equation, respectively.

Hydrodynamic equations

The laminar fluid flow equation of the incompressible fluid in the main flow channel which assumed with the density of the fluid is constant and the fluids are Newtonian with constant viscosity. By applying assumptions the systems are steady state, isothermal condition inside the channel and negligible body forces. The continuity (mass-balance) equation and the Navier-Stokes (momentum-balance) equations used for the flow in the domain outside the porous electrodes are given by:

$$\rho(\nabla \cdot \vec{u}) = 0 \tag{1}$$

$$\rho(\vec{u} \cdot \nabla \vec{u}) = -\nabla pI + \mu\left(\nabla^2 \vec{u} + \left(\nabla^2 \vec{u}\right)^T\right) \tag{2}$$

where $\vec{u}$ is the velocity vector, ρ is the fluid density, μ is the fluid viscosity, p is the static pressure. The carbon paper electrodes are treated as porous medium with homogeneous porosity and permeability in the in-plane direction. The pressure drop occurs within the electrodes is determined using the well-known Brinkman equation (Brinkman's extension from Darcy's law). The Darcy's pressure and velocity are dependent variables in the Brinkman equation. Brinkman equation includes the porosity in the permeability of the porous media which are used to account the consumption of the species. The fluid flow through porous media (gas diffusion layer) is modeled by incorporation of the continuity equation and momentum equation. Similarly, the continuity and momentum equations for regions inside the electrodes (for porous media) are given by:

$$\rho(\nabla \cdot \vec{u}) = 0 \tag{3}$$

$$\frac{\rho}{\varepsilon^2}(\vec{u} \cdot \nabla \vec{u}) = -\nabla p I - \frac{\mu}{k}\vec{u} + \nabla\left(\frac{\mu}{\varepsilon}\left(\nabla \vec{u} + (\nabla \vec{u})^{\mathrm{T}}\right) - \frac{2}{3}\frac{\mu}{\varepsilon}(\nabla \cdot \vec{u})I\right) \tag{4}$$

where ε is the porosity of the media, k is the permeability of the electrodes (catalyst layers and gas diffusion layers/porous electrodes).

Species transport equations

The reactant species as fuel and oxidant are transported along the channel by convection, while diffusive transport in a direction transverse to the flow is important to replace the reactant in the vicinity of the electrodes surface as they are consumed by electrochemical reaction. The diffusion rates can be assumed to be linearly proportional to concentration gradients while concentrations are sufficiently low, especially at low current densities and interactions between different solute species can be ignored. In addition, due to the fuel and oxidant solution are both dilute, so we use the physical properties of pure water where necessary. The mass transport of species is of pure convective-diffusive nature, the concentration distributions of the fuel and oxidant can be described by Fick's law [7,8] given as

$$\nabla \cdot (-D\nabla c + c\vec{u}) = 0 \tag{5}$$

where c is the local concentration of the species in the anode and cathode, D is the diffusion coefficient of the species which refers to the formic acid diffusivity in aqueous media (water and electrolyte) in the anode and the oxygen diffusivity through the porous electrodes in the cathode. In the catalyst layers domain where the species are consumed by electrochemical reactions, so they have a source term in the system. A source term is added to the mass transport equation abovementioned as follows:

$$\nabla \cdot (-D\nabla c + c\vec{u}) = \frac{e}{nF} \cdot i \tag{6}$$

where e is the mole number, n is the number of electrons transferred in the reaction, F is the Faraday constant, and i is the local charge transfer current density in the reaction, reflects the rate of the electrochemical reaction which is calculated through Butler-Volmer equations.

The oxygen concentration at the cathode is assumed to be constant. All the walls are set as zero flux boundary condition. The effective diffusion coefficient of species D_i^{eff} and the effective conductivity of the porous electrode σ_s^{eff} is determined by Bruggeman correction:

$$D_i^{eff} = \varepsilon^{3/2} \times D_i \tag{7}$$

$$\sigma_s^{eff} = (1-\varepsilon)^{3/2} \times \sigma_s \tag{8}$$

Charge equations

In this study, sulfuric acid (H$_2$SO$_4$) solutions was added to both anode and cathode electrolyte channel to serve sufficiency proton which protons transported from the anode to cathode is by electric migration only. The transport of charged species and the electric field within the electrode and the electrolyte can be modeled using the potential equation from the Secondary Current Distribution module of the COMSOL Multiphysics 5.1. Both the fuel and oxidant are dissolved in sulfuric acid electrolyte, the concentration of formic acid ions was assumed to be uniform along the channel. Transportation both proton and electron are controlled by electrolyte ionic potential and solid-phase electronic potential. In related to electrochemical reaction, the ionic current distribution flows in catalyst layer and

anode-cathode electrolyte, while the electronic current distribution flows in gas diffusion layer and catalyst layer. There is no electrochemical reaction in the gas diffusion layer, it means the source term of electronic current is set to be zero. The electronic potential in the solid-phase is described by:

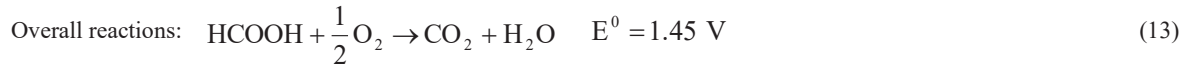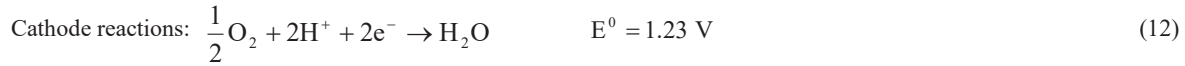$$\sigma_s \nabla \cdot \nabla \phi_s = 0 \qquad (9)$$

Similarly, the source term for the ionic current in the anode-cathode electrolyte should be zero and expressed as follows:

$$\sigma_l \nabla \cdot \nabla \phi_l = 0 \qquad (10)$$

Where σ_s is the electronic conductivity, ϕ_s is the over potential in catalyst layer, σ_l is the electrolyte conductivity, and ϕ_l is the electrolyte over potential. Applying a potential boundary conditions for the outside electrode walls resulted in an essentially uniform solid-phase potential over the entire electrode subdomain. The electric insulation boundary conditions were assigned to other boundaries. Subsequently, electric insulation boundary conditions were applied to all of the channel surfaces. In the electrodes, where charged species are generated or consumed. The current source is applied and the local current density is calculated by the Butler-Volmer reaction kinetics equations.

Electrochemical reaction kinetics

In this study, two electrochemical reactions corresponding standard electrode potential were considered. The fuel oxidation reaction of formic acid oxidation reaction takes place at the anode/catalyst layer surface while the oxygen-reduction reaction takes place at the cathode electrode:

Anode reactions: $\quad HCOOH \rightarrow CO_2 + 2H^+ + 2e^- \qquad E^0 = 0.22$ V $\qquad (11)$

Cathode reactions: $\quad \dfrac{1}{2}O_2 + 2H^+ + 2e^- \rightarrow H_2O \qquad E^0 = 1.23$ V $\qquad (12)$

Overall reactions: $\quad HCOOH + \dfrac{1}{2}O_2 \rightarrow CO_2 + H_2O \quad E^0 = 1.45$ V $\qquad (13)$

The Butler-Volmer equation is the fundamental relationship between the local current density across the electrode surface in the microfluidic fuel cell and related to both the applied electric potential and the concentration of reactant species, which describes the rate of an activation controlled reaction. In the original Butler-Volmer equation there is no concentration gradient term. However, in this study the Butler-Volmer reaction kinetics equation multiplied by the concentration term since the rate of the electrochemical reactions in microfluidic fuel cell is limited by mass transfer. The reaction rates are assumed to be linearly proportional to reactant concentration. At the concentrations are sufficiently low, interaction between different solute species can be ignored and diffusion rates can be assumed to be linearly proportional to concentration gradients. The rate of the reaction is controlled merely by the rate of the electrochemical charge transfer, as follow

$$i_{loc,a} = a i_{0,f} \left(\frac{C_f}{C_{f,ref}} \right)^{\beta} \left[\exp\left(\frac{\alpha_a nF}{RT} \eta \right) - \exp\left(\frac{\alpha_c nF}{RT} \eta \right) \right] \qquad (14)$$

here, $i_{loc,a}$ represents the local current density in the anode, a is the density of catalytic active area, $i_{0,f}$ is exchange current density at the anode, C_f is the local fuel concentration, $C_{f,ref}$ is the reference fuel concentration, β is the reaction order $(\beta = 1)$, α_a and α_c is the charge transfer coefficients, R is the ideal gas constant, T is absolute temperature, and η is the activation over potential on the electrodes to overcome irreversibilities, which is determined by

$$\eta_a = \phi_s - \phi_l - E_{eq} \qquad (15)$$

here ϕ_s and ϕ_l are the electric potential of anode catalyst layer and the local electrolyte potential derived from Eqs. (9) and (10), respectively, E_{eq} represents the equilibrium potential (reversible). In this model, the crossover is considered as a current density, with units of mA cm^{-2}. The crossover can be calculated using the formula:

$$i_{crossover} = nF M_{fuel} \qquad (16)$$

where n is the number of electrons transferred at the limiting step $(n=2)$, F is the Faraday constant $(96485\ C\,mol^{-1})$, and M_{fuel} is the molar flux of the fuel crossover at the electrolyte/cathode catalyst layer interface. In order to properly the electrochemical reaction in the cathode, fuel crossover is considered in the microfluidic fuel cells. The rate of reaction for the cathode is calculated by the following equation:

$$i_{loc,c} = ai_{0,o}\left(\frac{C_o}{C_{o,ref}}\right)^{\beta}\left[\exp\left(\frac{\alpha_a nF}{RT}\eta\right) - \exp\left(\frac{\alpha_c nF}{RT}\eta\right)\right] - nFM_{fuel\,crossover} \tag{17}$$

where, $i_{loc,c}$ represents the local current density in the cathode, $i_{0,o}$ is exchange current density at the cathode, C_o is the local oxygen concentration, $C_{o,ref}$ is the reference oxygen concentration, and η is the activation over potential on the electrodes to overcome irreversibilities, which is determined by

$$\eta_c = \phi_s - \phi_l - E_{eq} \tag{18}$$

here ϕ_s and ϕ_l are the electric potential of cathode catalyst layer and the local electrolyte potential. The equilibrium potential, E_{eq}, represents a constant value which is based on the electrochemical reaction Gibbs free energy change at standard operating conditions.

Boundary conditions

For simplification a three-dimensional numerical simulation analysis, boundary conditions are studied in the model development as follows in Table 2, used to solved the governing equations.

TABLE 2. Assumptions and boundary conditions used in the microfluidic fuel cell

Hydrodyamic boundary conditions:
(1) For Navier-Stokes equation, an initial velocity of fluid at the anode and the cathode channel inlet is constant;
(2) No-slip boundary condition is set for all the walls. So, the velocity for all channel walls is equal to zero.
(3) Volumetric flow rates are $0.05, 0.1, 0.3, 0.5, 0.7\ \text{mL/min}$ at the anode inlet;
(4) Pressure channel outlet is set equal to zero, and an external force and gravity effect are neglected because of viscous dissipation at a low velocity;
(5) Pressure point constraint was employed in air-breathing boundary outlet set to zero at the end of the cathode electrode bottom side;

Species transport boundary conditions:
(1) For convective/diffusive transport, in initial bulk concentration of fuel at the anode channel inlet are $0.3, 0.5, 1.0\ \text{M}$. While concentration of oxygen of air-breathing cathode inlet is $0.85\ \text{M}$. In addition, an initial oxygen concentration in the cathode channel inlet set to zero;
(2) For transport of dilute species domain, applying the diffusion and convection flux conditions through the outflow boundary conditions. Convective flux is set at the outlet channel, $n\cdot(-D\nabla c)=0$, This boundary states that diffusivity transport perpendicular to the normal boundary can be neglected. So that this boundary conditions vanishes concentration gradient in the fluid flow direction;
(3) For the no flux boundary conditions, no mass flow in or out of boundaries that the total flux is zero. As the equation represents that the mass flux of the species perpendicular to the boundary equals to zero, the walls are defined to be insulating, $n\cdot(-D\nabla c + cu)=0$.

Charge transport boundary conditions:
(1) To calculate the electric field, the ground potential is set for anode. The cathodic voltage is set as a variable, cell voltage E.
Anode voltage $\phi_a = 0$, and cathode voltage $\phi_c = E_{cell}$.

Parameters constant

The parameter operating conditions used in the three-dimensional computational model for air-breathing microfluidic fuel cells are listed in Table 3. Performance of microfluidic fuel cells can be predicted by solving the continuity, momentum, species transport and charge equations in the anode and the cathode, respectively, along with the channel of the microfluidic fuel cell using the governing equations in the catalyst layer and in the anolyte-catholyte.

TABLE 3. The physical/transport properties used in the model for numerical simulation

Parameters	Symbol	Values
Electrode properties:		
- Porosity & permeability of catalyst layer	ε, κ	0.3 & 2.36×10^{-12} m^2
- Porosity & permeability of gas diffusion layer	ε, κ	0.4 & 1.18×10^{-12} m^2
- Conductivity of electrode, S/m	σ_s	222
- Conductivity of electrolyte, S/m	σ_l	16.7
Fluid properties:		
- Density of anolyte and catholyte stream, kg/m^3	ρ	1000
- Dynamic viscosity, Pa.s	μ	0.001
- Volumetric flow rate, mL/min	v	0.05, 0.1, 0.3, 0.5, 0.7
- Temperature, K	T	298
- Faraday constant, C/mol	F	96485
- Reference concentration of formic acid, mol/m^3	$c_{0, HCOOH}$	300, 500, 1000
- Reference concentration of oxygen, mol/m^3	$c_{0, O2}$	85
- Diffusivity of formic acid as anolyte, m^2/s	D_{HCOOH}	2.546×10^{-9}
- Diffusivity of oxygen in water, m^2/s	$D_{O2(H2O)}$	2.1×10^{-9}
- Diffusivity of oxygen in air, m^2/s	$D_{O2 (air)}$	2.1×10^{-5}
Anodic and cathodic kinetic reactions:		
- Exchange current density at the anode, A/m^2	i_{oa}	2250
- Exchange current density at the cathode, A/m^2	i_{oc}	6×10^{-4}
- Anodic & cathodic charge transfer coefficient	α	0.5
- Number of transferred electrons at the anode & cathode	n	2

RESULTS AND DISCUSSION

COMSOL model validation

Numerical models of T-shape air-breathing MFCs was built with the same dimensions and operating conditions as the one from Shyu [8]. In this numerical study, the microchannel has a cross-sectional shape of the inlet and outlet of the same along the channel. Height and width of a microchannel have the same size and consistency throughout the channel. The size of the channel, for two inlets are the same length and have opposite directions. The results of numerical simulation for the polarization curves on the anode and cathode electrode are obtained that the agreement between experiment with measured data and the numerical simulation data is fit well and reasonably good, which confirm the reliability and effectiveness of the model as shown in Fig. 3 (a). Therefore, the present model of the air-breathing microfluidic fuel cells are validated. In addition, the parameter studies such as proton conductivity, exchange current density, and the oxygen concentration has maintained always a constant, while the volumetric flow rate and the fuel concentration are the condition parameters that can be changed. Furthermore, the model used to analyze polarization behaviors on the electrode and the cell performance in order to obtain the numerical model appropriate for governing equation of the present model, which is discussed below in detailed.

In the numerical simulation value of the fuel cell as shown in Fig. 3 (b-d), with a fuel concentration of 0.5 M, the maximum power density of the fuel cell was approximately 17.15 mW/cm^2, 19.81 mW/cm^2, and 25.65 mW/cm^2 at 0.05 mL/min, 0.1 mL/min, and 0.5 mL/min, respectively. The cell performance has a maximum power density of 36.78 mW/cm^2 at a current density of 105.1 mA/cm^2 at a fluid volumetric flow rate of 0.5 mL/min. The cell performance increases along with increasing fluid flow velocity of the microchannel cell. This will enhance fuel crossover at the cathode consequently, it will decrease a concentration of anolyte and catholyte stream.

The performance of I-V and power density curve are presented in Fig. 3 (a-d), respectively. Explicitly, the cell performance I-V and power density rise gradually in the concentration of fuel. The exchange current density on electrode of each curve in Fig. 3 (b-d) are not proportional to the concentration of fuel as well as the maximum power density. As in the case of the cell performance for 0.5 M-HCOOH with volumetric flow rate of 0.5 mL/min in Fig. 3 (b-d), the cell current density on anode electrode increases from 96.27, 112.29, and 148.53 mA/cm^2, respectively, only as the fuel concentration increase from 0.3 M to 1 M-HCOOH at the proton conductivity of 16.7 S/m. In this case indicate that even though a stronger volumetric flow rate can enhance the transport of fuel to the anode electrode, this influence alleviates gradually and the concentration loss because of the inadequate transport of oxygen from ambient

air into gas diffusion layer to the cathode electrode surface occurs lastly. In general, stronger volumetric flow rate and concentration will increase the cell performance, including the cell current density and the cell power density.
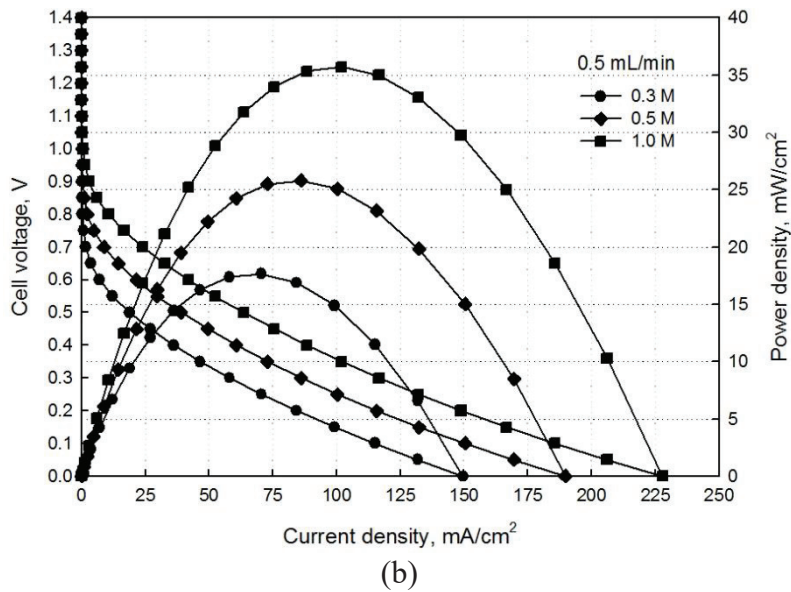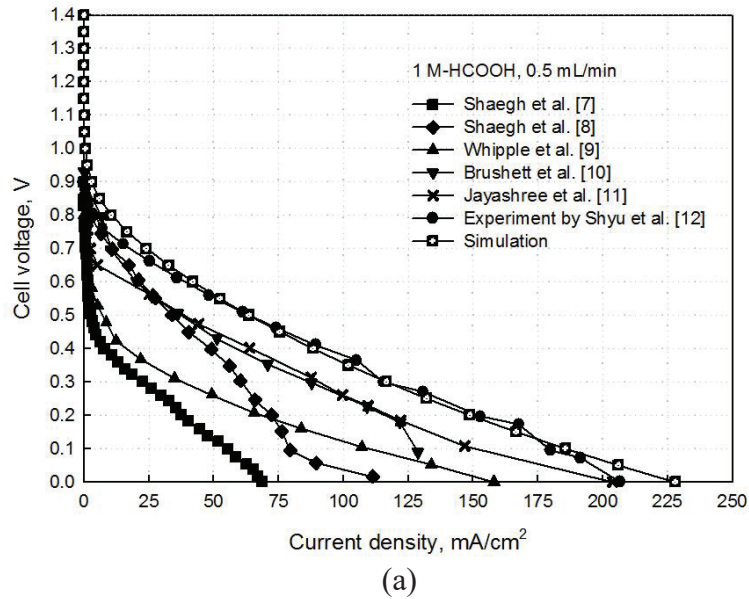

(a)

(b)

FIGURE 4. The overall performance air-breathing MFCs: (a) Performance comparison between the experimental vs simulation (1.0 M-HCOOH, 0.5 mL/min) and other published data; (b) V-I and P-I curves of the fuel cell operated at [HCOOH] = 0.3 M, 0.5 M, and 1.0 M with the volumetric flow rate of 0.05 mL/min, 0.1 mL/min and 0.5 mL/min

Overvoltage on the Electrode

The cell performance corresponding with the rate of electrochemical reaction kinetics in Eq. (9) and Eq. (10), which activation overvoltage and species concentration values must be given for the anode and cathode electrode. The

performance of a fuel cell is described by a graph of both the cell voltage output and current density on the electrode in Fig. 4 (a). Firstly, is most of an important characteristic of the fuel cell to obtain the I-V curve or polarization curve, set of the cell voltage is fixed and the cell current is accounted the corresponding with Eq. (9), to get the local current density on the electrode of the cell and different polarization losses of the cell performance. At a low load region seems a large drop of equilibrium voltage of 1.45 V to the cell voltage around 0.9 V. In the microfluidic fuel cells, the cell voltage output is always less than the open circuit voltage due to irreversible losses. Based on the graphical performance of the cell, these losses will increase as more current and together with a decreasing voltage output of the cell. The irreversible losses known as overpotential or overvoltage of the cell are caused by the following factors: activation overvoltage because of kinetic of the electrochemical reactions at the anode and cathode electrode, ohm overvoltage because of internal charge transport, and concentration overvoltage because of mass transport limitation on the electrode. The kinetic losses at the electrode due to the low reaction kinetic of oxygen reduction on the cathode side which generate overvoltage to obtain the current density. Subsequently, the kinetic losses continue to take place on the catalyst layer will increase the load and generate ohmic losses due to the internal resistance of the cell (in electrolyte and electrode). In this case added the electrolyte to support the electron in the reaction. Finally, a high current density generates a little bit drop of voltage due to concentration losses which the reactant (fuel and oxidant) sluggish delivered to the catalyst layer. It means that there were no diffusion reactions in the gas diffusion electrode region.

The operating cell voltage output is equal to the open circuit voltage reduced by voltage drop or the potential losses, by the following equation:

$$V_{cell} = V_{ocv} - (\Delta V_{act} + \Delta V_{fc} + \Delta V_{ohm} + \Delta V_{conc}) \tag{19}$$

where, V_{cell} is the cell voltage for a certain operating condition, V_{ocv} is the operating circuit voltage of the fuel cell in this experiment. While V_{act} is the voltage drop associated with the activation of the anode and cathode electrode which are obtained from the simulation, ΔV_{fc} is the fuel crossover at a low current densities, V_{ohm} is the ohmic voltage drop associated with the conduction of protons and electrons, and V_{conc} is the voltage drop resulting from the decrease in the concentration of fuel and oxidant on the electrode that is eliminated in this experiment.

The present study, the equilibrium voltage used in this simulation is 1.45 V corresponds with redox reactions of the formic acid and the oxygen. In this condition that the cell voltage has zero current and not connected to any load in the circuit. The simulation and experimental data as shown in Fig. 4 (a), there is no drop sharply of the cell voltage at a higher current densities for certain operating conditions in this experiment. For simplifying the simulation modeling, therefore the above mentioned the concentration overvoltage can be neglected. Likewise with the experimental data and the simulation of cell disclosed the open circuit voltage between 0.9 V to 1.45 V. Because almost there is no the drop of the open circuit voltage at a low current densities for a given operating condition, then accordingly the fuel crossover in Eq. (19) can be eliminated, known as the ideal operating point of current distribution in the fuel cell. Overvoltage on both the anode and the cathode electrode used to reduce the open circuit voltage that is generated from experimental data. Then, the simplification in Eq. (20) based on the experimental data as follows

$$V_{cell} = V_{ocv} - (\Delta V_{act} + \Delta V_{ohm}) \tag{20}$$

To determine the proton conductivity value that across the interface from the anode and cathode channel, for the fuel 0.5 M of formic acid mixed with 0.5 M sulfuric acid. Based on the table of conductivity versus concentration for solutions at 25^0C operating conditions, the proton conductivity value of 0.5 M sulfuric acid was measured to be 16.7 S/m. The proton conductivity is an important function of anode fuel concentration [1,7].

Velocity distribution

Navier-Stokes equations describe the velocity and pressure distribution in the microchannel. Boundary conditions for both equations are applied into the model. For the avier-Stokes equations, an initial velocity is defined which fluid is introduced into the microchannel $(u = u_0)$, the velocityat the walls is equal to zero, referred to as the no slip conditions $(u = 0)$, and the pressure is defined to be zero at the outlet channel $(p = 0)$.
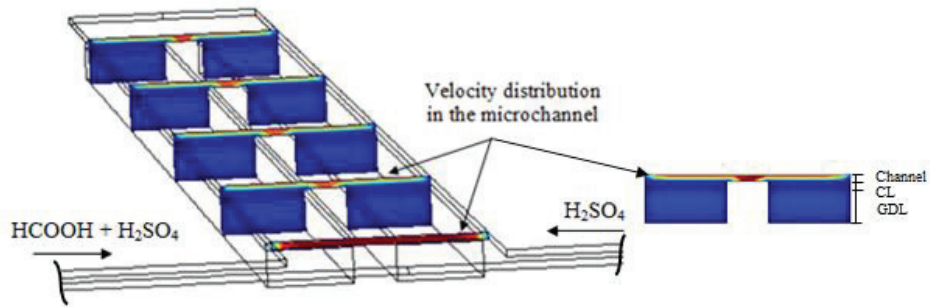
FIGURE 5. Velocity distribution profiles of fuel along the microchannel at 0.167 m/s with [HCOOH] = 0.5 M placed on the *z-x* planes with number planes of 5 pieces

Fuel concentration distribution

The cell performance evaluated by a change of fuel concentration and oxygen concentration in the microchannel. Since the microfluidic fuel cell running on laminar flow, changes in the laminar flow velocity in the microchannel will effect of reactant transport and fuel cell performance. Depletion of fuel occurs at a high volumetric flow rate is replenished by the fuel stream rapidly. The fuel concentration profiles have the diffusion region becomes to change and moves to the channel outlet along with the volumetric flow rate increasing, that will cause depletion fuel at the cathode channel outlet. The fuel losses at the channel outlet caused by mixed diffusion of different concentration and a high volumetric flow rate along with microchannel can be shown in Fig. 7 (a). For volumetric flow rate decrease will cause accelerated mixing diffusion of reactant. While a higher fuel concentration of 1 M, mixed diffusion minimum can be resulted in 0.5 mL/min.
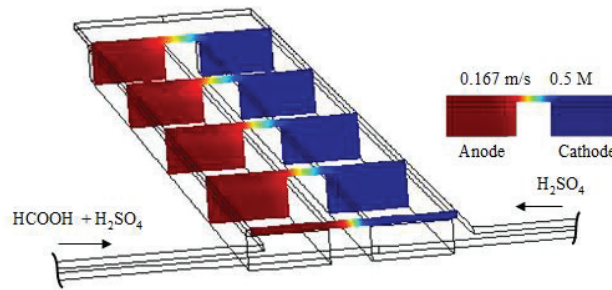

FIGURE 6. HCOOH concentration distribution profiles along the microchannel at 0.167 m/s with [HCOOH] = 0.5 M placed on the *z-x* planes with number planes of 5 pieces
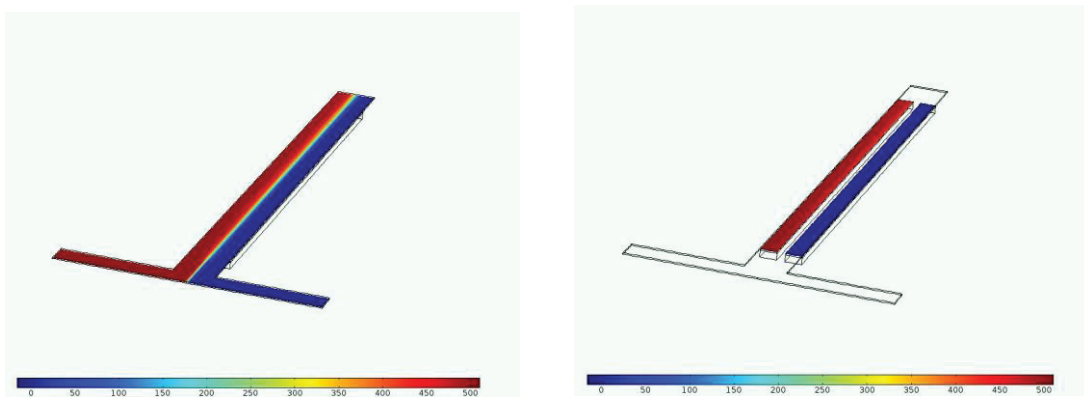

FIGURE 7. The concentration distribution of formic acid along the microchannel at 0.167 m/s with inlet [HCOOH] = 0.5 M: (a) on the electrode surface; (b) on the mid-plane along the channel

The concentration of fuel on the mid-plane along the channel results in Fig. 7 (a) reveals that in the beginning mixing of fuel at lower diffusive in the interface at the anode and cathode stream at a high formic acid flow rate provide a higher concentration of formic acid in the anode stream leading to the decrease of concentration losses. Based on the result of numerical simulation also presents that at a high fuel flow rate with lower diffusive mixing indicates the decrease of concentration losses due to higher fuel concentration at the anode channel side. The zone of concentration losses on the electrode surface revealed in Fig. 7 (b) that the depletion boundary layer of fuel due to the consumption rate a higher concentration loss. In this study, based on the experimental data for the open circuit voltage is in the range of 0.9 to 1.45 V. The performance of cells is also affected by changes in a volumetric flow rate will affect the process of diffusion and transport of reactants in the microchannel. It seems at a lower the flow rate of fuel, the diffusion process of fuel and oxidant along the channel will decrease. It is accompanied by a fuel concentration value decreasing move to downstream (the output channel), then diffusion gradually thinning at the end of the channel as shown in Fig. 6. At a high volumetric flow rate (Q_3), the feeding of 0.5 mL/min, the diffusion region is very strong zone at the beginning of the channel. The depletion boundary layer caused by the fuel consumption over the anode electrode. The stream rapidly replenishes depletion of the fuel while the formation of the region with a low fuel concentration due to decreasing of the volumetric flow rates. While the fuel concentration distribution of the very low volumetric flow rate of Q_1 shows that the growth of the depletion layer on electrode surface inside the microchannel seems obvious. While the volumetric flow rate of 0.1 mL/min and 0.05 mL/min diffusion of fuel is clearly visible in the liquid interface or the middle of the channel, where the fuel across and reach the cathode side through electrolyte stream.
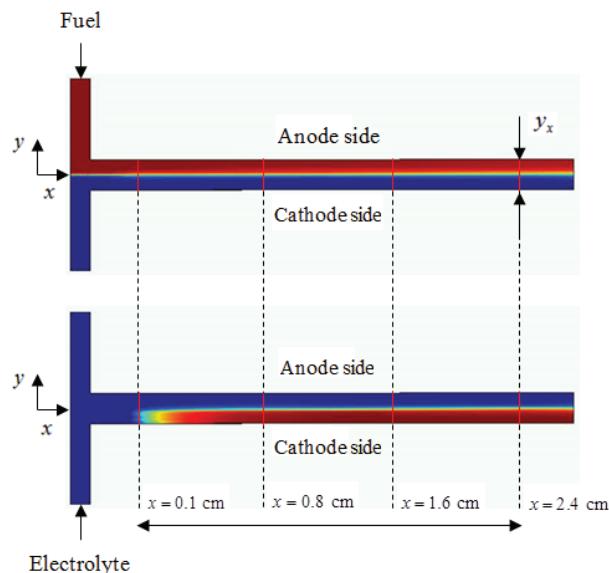

FIGURE 8. Concentration distribution of formic acid for volumetric flow rate of 0.5 mL/min with [HCOOH] = 0.5 M placed on the *y-z* plane at 4 specific positions of width coordinate of the microchannel

Analysis of the concentration distribution over the electrode inside the microchannel as shown in Fig. 8, which width of the microchannel (y_x) and the width coordinate of the microchannel (x) along the microchannel of $x = 0.1$, 0.8, 1.6 and 2.4 cm at a volumetric flow rate of 0.05 mL/min seems like the growth of the depletion interface layer between fuel and oxidant stream over the electrode. This occurs due to a decrease in flow rate in the microchannel, which will produce low-concentration fuel region. While at a high volumetric flow rate of 0.5 mL/min the fuel depletion occurs due to increased stream rapidly in the anode channel. The overall fuel consumption over the anode porous electrode generates a depletion boundary layer along the microchannel.

Fuel concentration distribution on the electrode surface at volumetric flow rate of 0.5 mL/min is 200 mol/m³, that is, a lower than fuel concentration on the mid-plane channel around of 250 mol/m³ as shown in Fig. 9 and Fig.10. In this case due to the electrochemical reaction takes place on the electrode need more fuel consumed than on the mid-plane along the microchannel. It is important to know the current distribution in the cathode catalyst layer

corresponding to the performance of the electrode in the cell. The current distribution through the cathode catalyst layer can be obtained by experiments and simulation based on electrochemistry and species transport theory. The constant parameters in Table 3 were employed to simulate the current distribution through the cathode catalyst layer. The current density distribution occurs in the cell can be caused by non-balanced of the oxygen diffusion process on the surface of the cathode catalyst layer, as described in Fig. 9 and Fig.10.
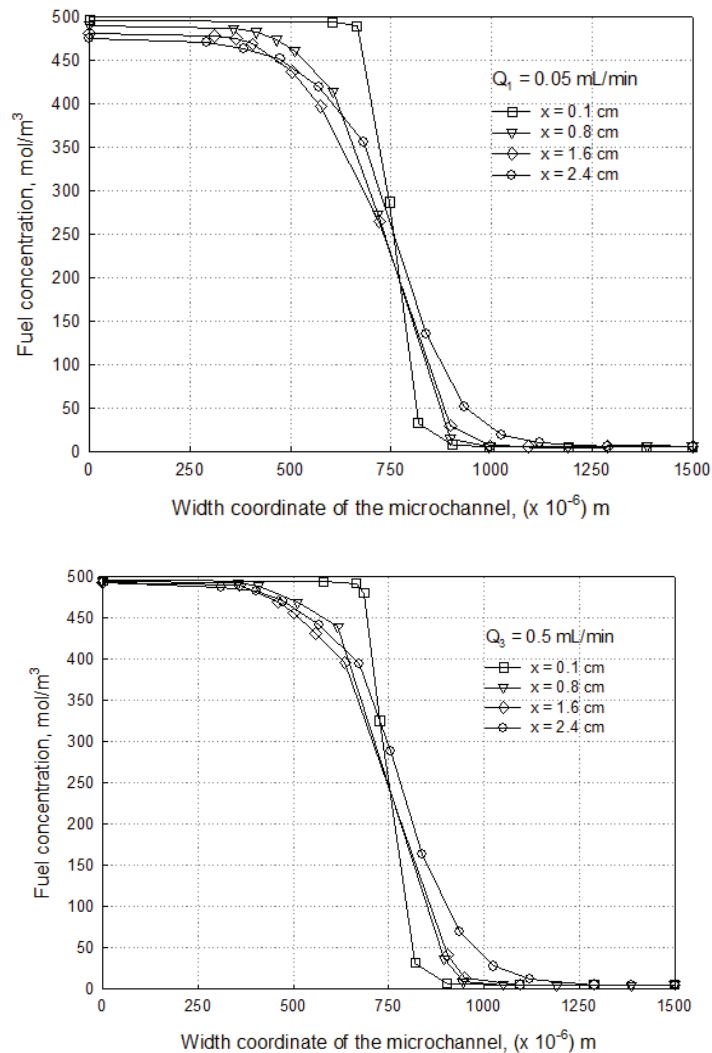

FIGURE. 9. The formic acid concentration distribution along the microchannel at 4 specific positions of width coordinate of the channel with inlet [HCOOH] = 0.5 M on electrode surface of the microchannel: (a) flow rate of 0.05 mL/min; (b) flow rate of 0.5 mL/min
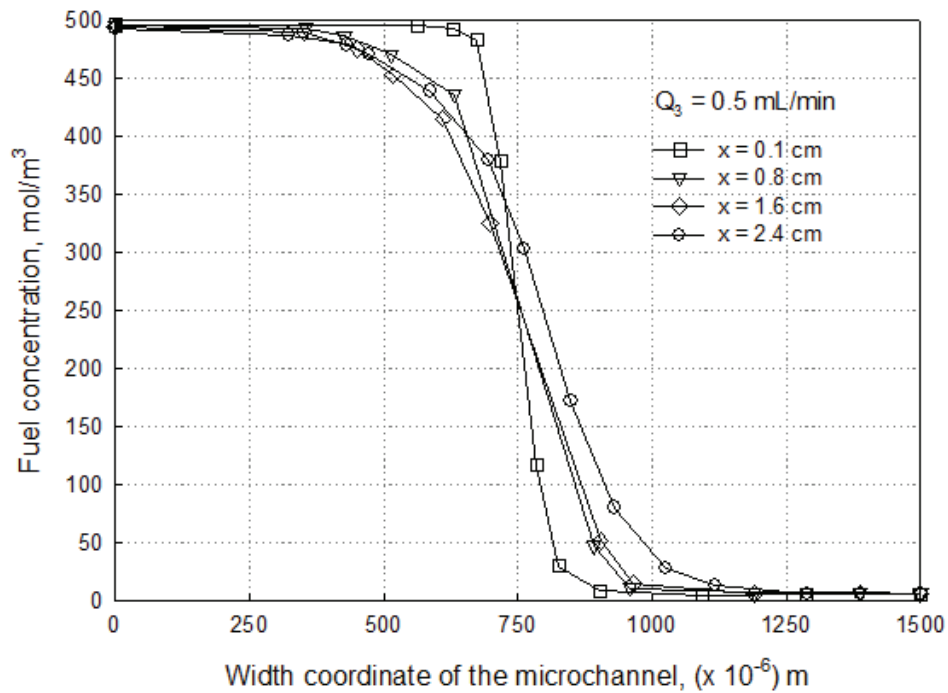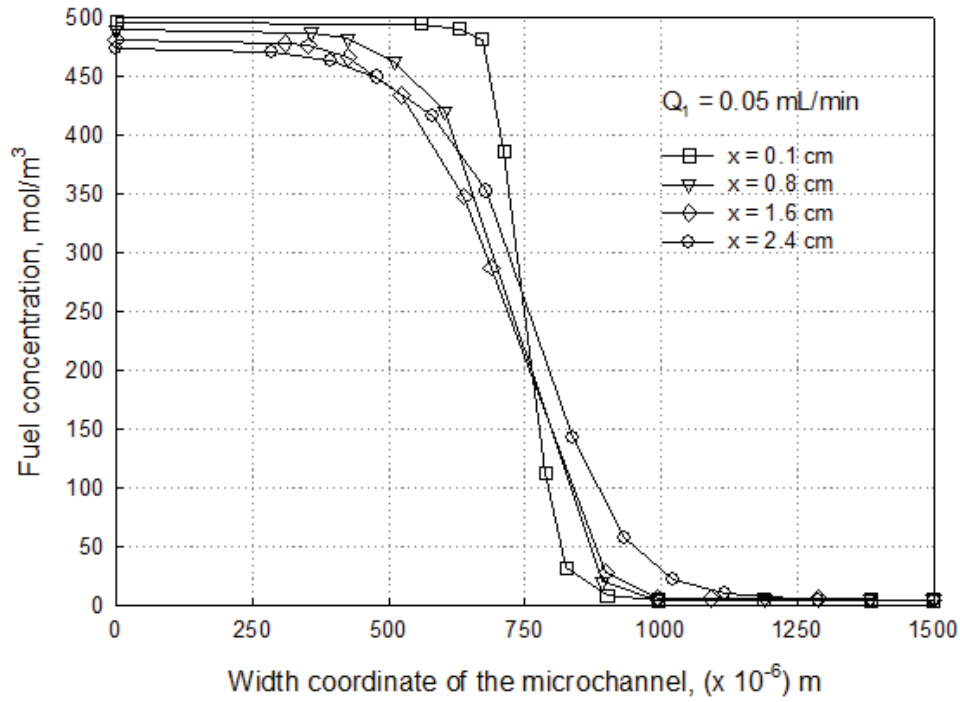
FIGURE 10. The formic acid concentration distribution along the microchannel at 4 specific positions of width coordinate of the channel with inlet [HCOOH] = 0.5 M at 0.5 mL/min on the mid-plane along the microchannel: (a) flow rate of 0.05 mL/min; (b) flow rate of 0.5 mL/min.

The above mentioned results indicates that the performance of the microfluidic fuel cell depends on the proton conductivity due to limitations generated at the anode and travels to reach the cathode electrode known as fuel crossover. The limitation of the proton conductivity can be improved by adding sulfuric acid solution to the cathode and/or anode stream in order to supply of proton closer toward a cathode electrode while still preserving a proton gradient because of consumption of protons at the cathode electrode. So that, the fuel crossover is important because occur at lower volumetric flow rates. The effect of fuel crossover of the cell performance of the anolyte stream can decrease fuel concentration and result in decreasing the current density. In addition, the electro-oxidation reaction of the formic acid on the cathode electrode surface inside the channel can lead to a mixed voltage and reduces the open circuit voltage. In the numerical simulation shows that the major reason for the sharp drop of open circuit voltage from 0.9 V with Q_3 to 0.8 V with Q_1 is the mixed voltage at the cathode side and fuel crossover losses at a lower volumetric flow rate.

Local current distribution on the electrode surface

An experimental study in Fig. 4 (a) indicates that the cell voltage decreases slowly along with increasing current density at a given operating conditions which there is no significant drop in the cell voltage. This means that the effect of the concentration overpotential in the numerical simulation can be neglected. Corresponding with electrochemical kinetic reactions in Eq. (8), that the electrode performance is shown by the rate of formic acid oxidation reaction on the anode and the reduction reaction of oxygen on the cathode. The simulated polarization curve described that all curves seem the parallel stripe indicating the same resistance value at certain current densities. The resistance losses are determined by electrolyte conductivity of concentration in sulfuric acid solution, the conductivity of the electrode, external electrical interconnection, and the electrode spacing between the anode and cathode.
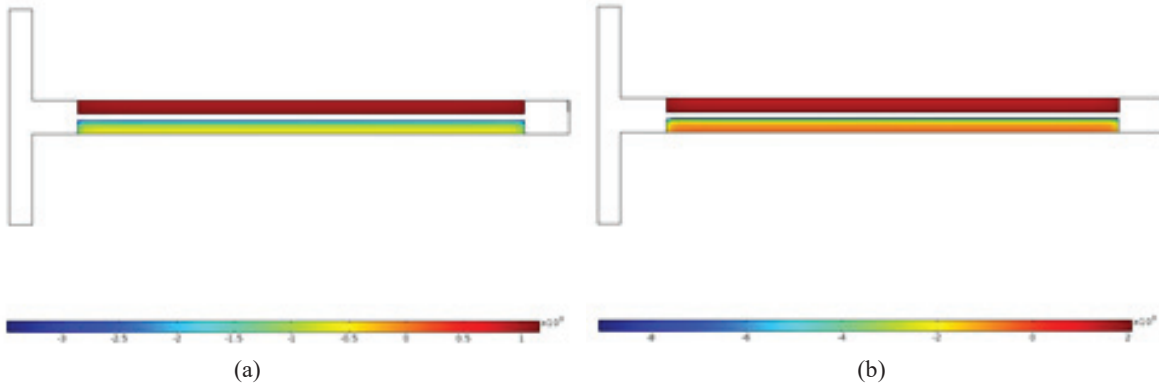

| (a) | (b) |

FIGURE 11. The local current distribution on electrode surface along the microchannel with inlet [HCOOH] = 0.5 M: (a) volumetric flow rate of 0.05 mL/min; (b) volumetric flow rate of 0.5 mL/min

The cell performance is described in terms of the polarization curve in Fig. 4 (a). The results of the cell performance good agreement with the experimental data in the intermediate and high current density distribution zone. The difference at low current densities are related to the experimental data at lower densities was inadequate. In the measured data curve in this zone is curve fitted to the higher current density data. The current distribution of the microfluidic fuel cell has reflected the transfer of ions from anolyte streams in the anode catalyst layer move to cathode catalyst layer and vice versa. This phenomenon results in a high value of current at the interface between the catholyte streams and cathode catalyst layer. Conversely, results in a minimum current at the interface between the cathode catalyst and gas diffusion layer. In this case, the ions are consumed cause the oxygen reduction reaction passes through a thickness of the cathode catalyst layer. The current distribution tends toward the liquid interface if a high ionic resistance within the cathode catalyst layer electrolyte. The the ionic resistance results in higher activation losses.

Fig. 12 shows that the current density in the mid-plane of the microchannel of 516.68 A/m² is generated from width coordinate of the microchannel $x = 0.3$ cm, for 457.98 A/m² is generated from $x = 1.25$ cm, and for 531.83 A/m² from $x = 2.2$ cm in the cathode catalyst layer. While in Fig. 13 presents that the current density on the electrode surface of the microfluidic fuel cell of 775.73 A/m² is generated from width coordinate of the microchannel $x = 0.3$

cm, for $627.32\ \text{A/m}^2$ is generated from $x = 1.25$ cm, and for $815.31\ \text{A/m}^2$ from $x = 2.2$ cm in the cathode catalyst layer. Based on the oxygen reduction reaction current distribution follows Tafel cathodic kinetics revealed that at high current densities there is an increase in the utilization of the catalytic consumption through the cathode catalyst.

The current distribution generated on the electrode surfaces lower than the current distribution generated in the mid-plane along the channel due to the current that generated on the electrode surface closer to the catalyst layer in the electrochemical reaction process. As well as in Fig. 12 and Fig. 13, the current density of the cathode electrode is negative, this matter corresponds to the oxidation reduction reaction where the electron leaves the cathode electrode move to the anode electrode. In this case, considering the cathode electrode has a negative overvoltage in which the actual voltage is lower than the reversible voltage, so the oxygen reduction reaction that dominates. In the operating fuel cell, the reduction of oxygen takes place of the cathode electrode. Moreover, the oxygen reduction of the cathode reaction needs a more significant overvoltage than the anode reaction. Then, the cell performance overall could be represented by only one of the exponential terms in Eq. (8) for solve the overvoltage at a given current density.

At low flow rates, a little number of fuel passing through the electrolyte and electron conduction through the electrolyte is known as fuel crossover. The current density decrease due to the concentration of fuel in anolyte stream decreases. The electrochemical oxidation reaction of fuel over the cathode can generate in a mixed voltage loss and drop the open circuit voltage. In this study, numerical simulation model reveals that the drop of the open circuit voltage at a volumetric flow rate of 0.5 to 0.05 mL/min are almost zero, as shown in Fig. 4 (a). In Fig. 12 and Fig. 13 shows the local current density distribution on the surface of the anode and cathode catalyst layer (in the y-z plane) with voltage 0.4 V with an inlet of 0.5 M-HCOOH. The performance of the local current density depends on the amount of the oxygen that transported to the catalyst layer. The current density distribution that affected by oxygen diffusion, seem uniform on the surface of the cathode catalyst. The local current density on the surface of the cathode catalyst layer is smaller than at the anode catalyst layer due to limitations of the diffusion that the reaction on the surface can not be employed fully. The current density of the electrode is affected by forced convection as described in Eq. (2). The current density distribution along the side edge of the anode electrode is higher because the oxygen concentration gradient across. The local current density distribution in the air-breathing microfluidic fuel cell is described in Fig. 12 and Fig. 13.

The results numerically show that a high mass transport resistance leads to high current densities but a low ionic resistance. The current distribution in the cathode catalyst layer reaches a maximum current as a function of the mass transport resistance, the ionic resistance, and charge transfer resistance. This means that the maximum current distribution in the cell is a function of the maximum depletion of the oxygen concentration in the outlet side of the channel and also the amount of the oxygen can be reacted and brought to the electrode surface of the mass transfer conditions. The increase current density corresponding to a decrease in oxygen concentration in the cathode catalyst layer. It seems that the local current density is almost uniformly shifted to the right side on the surface of the anode electrode.
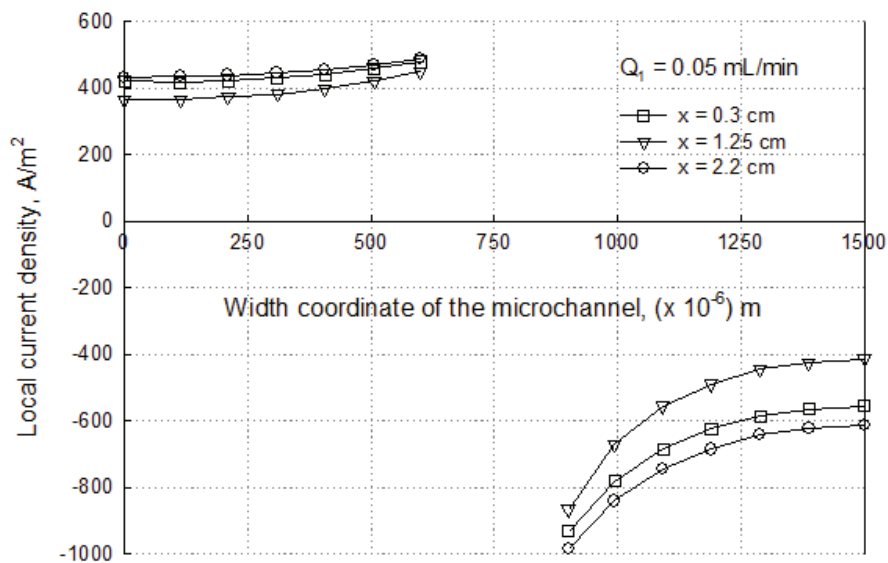

FIGURE 12. The local current distribution on electrode surface at 3 specific positions of width coordinate of the microchannel (x) with inlet [HCOOH] = 0.5 M at 0.05 mL/min
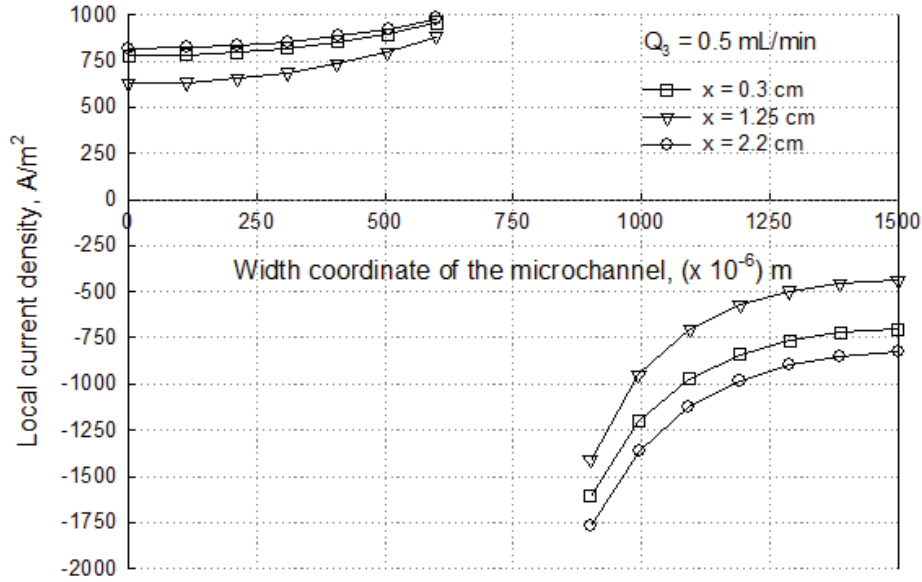
FIGURE 13. The local current distribution on electrode surface at 3 specific positions of width coordinate of the channel (x) with inlet [HCOOH] = 0.5 M at 0.5 mL/min

The local current density is low near the inlet, and gradually increases along the flow channel toward the channel middle, then decreases in the region near the outlet. The cell performance is higher in near the inlet region related to better electrolyte conductivity (lower ohmic overvoltage). The cell performance is lower in near the outlet because of higher the water flooding in the cathode channel side. At a higher water content in the cathode catalyst layer the mass transport limitations in the gas diffusion layer will be reduced and conversely.

The fuel utilization and Power Density

Based on the Eq. (21) represent that the amount of current fuel cell generated on the anode electrode depends on the fuel concentration. In addition, at a low flow rate and a lower fuel concentration on the anode electrode surface leading to low power density due to having the low open circuit voltage.
Fuel utilization can be presented as [12]

$$\varepsilon_{fuel} = \frac{I}{nFQ_{fuel}} \tag{21}$$

In here, I is the current generated by the fuel cell at 0.4 V, n is number of transferred electrons at the electrode ($n = 2$), F is the Faraday constant ($F = 96485 C/mol$), Q_{fuel} represents the fuel rate which is supplied to the fuel cell in unit of mol/s.

Fig. 14 shows performance fuel cell between fuel utilization and maximum power density under different conditions of volumetric flow rate which have affected by raising the volumetric flow rate ranging from 0.1 mL/min to 0.7 mL/min. At a higher flow rate will increase power density because the lower mixed voltage at the cathode side can generate a higher voltage. Besides the influence of the higher availability of reactant on the electrode surface active area and a higher volumetric flow rate of the electrochemical reaction can increase the current generated by the fuel cell. Based on the cell performance of the experiment and numerical simulation, which were the maximum power density of the microfluidic fuel cell always occurred at a voltage between 0.3 V and 0.4 V, the faster sharp drop of voltage in V-I curve at a higher volumetric flow rate to lower flow rate, which was 0.7 mL/min than 0.6 mL/min and 0.5 mL/min at 0.4 V.
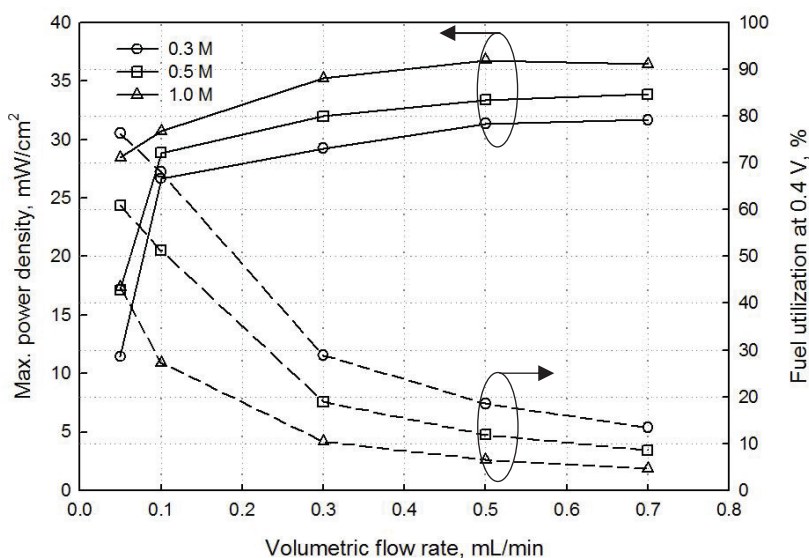
FIGURE 14. Maximum power density and fuel utilization (experiment versus simulation) of the microfluidic fuel cell at formic acid concentration of 0.3 , 0.5 M, and 1.0 M at various volumetric flow rates of 0.05, 0.1, 0.3, 0.5, and 0.7 mL/min.

As Figure 14 illustrates that the fuel utilization for each fuel concentration reduced as the flow rate increased, while the maximum power density increased as the flow rate increased, until it reached at a volumetric flow rate of 0.5 mL/min. For the volumetric flow rates of 0.1, 0.3, 0.5 and 0.7 mL/min with concentration of 0.5 M, the numerical simulation fuel utilizations of the fuel cell at maximum power density are 8.9, 7.95, and 7.2%, respectively. As a comparison for the fuel utilization performance proposed by Jayashree et al. [11], which was 7.5% at max. power density and fuel utilization are 31 mW/cm² and 0.8 mL/min, respectively. Shaegh et al. [8] was also the way to let the air-breathing microfluidic fuel cell have a peak power density of 20.5 mW/cm² at a volumetric flow rate and fuel utilization are 0.2 mL/min and 14%, respectively, for flow-through anode architecture of an air-breathing LFFC. The power density of the fuel cell can be enhanced by reducing the electrode spacing distance which lowers the cell resistance. Nevertheless, too small of an electrode spacing will enhance fuel crossover. Increasing fuel concentration and flow rates also will increase maximum power density and enhance performance mass transport to the anode through a thinner depletion boundary layer. For the same volumetric flow rates and concentrations, the experimental fuel utilizations of the fuel cell at the corresponding maximum power density are 8.75, 6.9, and 5.75%. It was evidence which there was a fit well and reasonably a good trend between numerical simulation and experimental results.

Likewise, for the experiment of the volumetric flow rate of the laminar streams will decrease from 0.7, 0.5, 0.3 and 0.1 mL/min, the corresponding maximum power density only drops from approximately 36.42 to 26.67 mW/cm², the fuel utilization increases from 5.9 to 8.75%. In the experiment as in a numerical simulation that the concentration losses can decrease the cell voltage at high current densities, especially operated with a flow rate of 0.05 mL/min which was fuel utilization of 2.33%. Fuel utilization also can be enhanced by reducing the flow rates at longer residence times, but the power density will be slightly decreased. Experimental data and numerical simulation obviously show that a higher fuel flow rate causes a high power density but a low fuel utilization.

CONCLUSION

Various effects on the performance of an air-breathing direct formic acid microfluidic fuel cell was simulated and measured in the present study. A three-dimensional numerical simulation is built for direct formic acid microfluidic fuel cells with flow-over on the surface of the anode-cathode electrode that breathes air as oxidant on the cathode bottom side. The present computational model simulation is validated towards the measured and others published data.

The dimension of the air-breathing direct formic acid microfluidic fuel cells having a 25-mm-long, 1.5-mm-wide, and 0.05-mm-deep microchannel. The spacing between two 25- mm-long, 0.6-mm-wide and 250-µm-thick cathode GDEs and 900 -µm-thick anode GDEs in a fuel cell was 0.3 mm. The formic acid of 0.3 M, 0.5 M, and 1.0 M mixed with 0.5 M-H_2SO_4 was used as fuel, which was varied at a volumetric flow rate of 0.05 mL/min, 0.1 mL/min, and 0.5 mL/min, another inlet a stream of 0.5 M-H_2SO_4 as an electrolyte and ambient air was breathed as an oxidant for generating electrical current.

The results in this study represented measuring experiment and numerical simulation which performance HCOOH concentration of 0.5 M the maximum power density of the fuel at 0.5 0.6, 0.7 mL/min for experimental was approximately 31, 32.16, and 31 mW/cm^2, respectively, while the maximum power density of the fuel at 0.5 mL/min, for numerical simulation was approximately 21.34, 25.65, and 36.78 mW/cm^2, respectively. The result of the present study reveals that the cell open circuit potential slightly increased along with the increase of the fluid flow rate on the fuel reactant solution. The fuel mass transport pass through a microchannel above anode electrode is limited by species mass transfer and will enhance proton crossover in the cell. The major effects of proton/fuel crossover are a decrease of open circuit potential, and reduce the concentration of fuel above the anode electrode caused by mixing potential. In addition, that performance microfluidic fuel cells are affected by five factors, including electrolyte concentration, reactant concentration, microchannel geometry, fluid flow rate, electrode arrangement. This model presents concepts into the couple mass transport process and electrochemical reaction kinetics of an air-breathing microfluidic fuel cells, and can guidance future design and optimization. The local current density in the microfluidic fuel cells with different operating conditions of flow rate and concentration have experimentally measured and numerical simulation. The optimum cell performance occurs in the electrode region that have the most of the average distributed current density profiles.

Further work in this field is the development, enhancement, and continued improvement, including modify microchannel design, flow type, and fuel type of an air-breathing microfluidic fuel cell in the near future to obtain the cell performance (fuel utilization and power density) as a function all of the relevant parameters constant. In addition, in connection with the performance of fuel cells is necessary to develop a study of bubble formation inside the microchannel.

ACKNOWLEDGMENTS

REFERENCES

1. E. Kjeang, N. Djilali, D. Sinton, Journal of Power Sources, **186**, 353-369 (2009).
2. H. Xu, H. Zhang, H. Wang, D.Y.C. Leung, L. Zhang, J. Cao, K. Jiao, J. Xuan, Applied Energy, **160**, 930-936 (2015).
3. K.J. Jeong, C.M. Miese, J.H. Choi, J. Lee, J. Han, S.P. Yoon, S.W. Nam, T.H. Lim, T.G. Lee, , Journal of Power Sources, **168**, 119-125 (2007).
4. A. Bazylak, D. Sinton, N. Djilali, Journal of Power Sources **143**, 57-66 (2005).
5. B. Zhang, D.D. Ye, P.C. Sui, N. Djilali, X. Zhu. Journal of Power Sources **259**, 15-24 (2014).
6. A.E. Khabbazi, A.J. Richards, M. Hoorfar, Journal of Power Sources **195**, 8141-8151 (2010).
7. S.A.M. Shaegh, N.T. Nguyen, S.H. Chan, Journal of Micromechanics and Microengineering **20**, 105008 (12pp) (2010).
8. S.A.M. Shaegh, N.T. Nguyen, S.H. Chan, W. Zhou, Journal of Hydrogen Energy **37**, 3466-3476 (2012).
9. H. Zhang, J. Xuan, H. Xu, M.K.H. Leung, H. Wang, D.Y.C. Leung, L. Zhang, X. Lu, Energy Procedia **61**, 250-253 (2014).
10. F.R. Brushett, R.S. Jayashree, W.P. Zhou, P.J.A. Kenis, Electrochimica Acta **54**, 7099-7105 (2009).
11. R.S. Jayashree, S.K. Yoon, F.R. Brushett, P.O. Lopez-Montesinos, D. Natarajan, L.J. Markoski, P.J.A. Kenis, Journal of Power Sources **195**, 3569-3578 (2010).
12. J.C. Shyu, P.Y. Wang, C.L. Lee, S.C. Chang, T.S. Sheu, C.H. Kuo, K.L. Huang, Z.Y. Yang, Energies **8**, 2082-2096 (2015).
13. J.C. Shyu, C.L. Huang, T.S. Sheu, H. Ay, Micro and Nano Letters **7**, 740-743 (2012).

14. R.S. Jayashree, L. Gancs, E.R. Choban, A. Primak, D. Natarajan, L.J. Markoski, P.J.A Kenis, Journal of the American Chemical Society **127**, 16758-16759 (2005).
15. R.S. Jayashree, D. Egas, J.S. Spendelow, D. Natarajan, L.J. Markoski, P.J.A. Kenis, Electrochemical and Solid-State Letters **9**, A252-A256 (2006).
16. H. Zhang, J. Xuan, H. Xu, M.K.H. Leung, H. Wang, D.Y.C. Leung, L. Zhang, X. Lu, Energy Procedia **61**, 250-253 (2012).
17. H. Wang, D.Y.C. Leung, J. Xuan, International Journal of Hydrogen Energy **36,** 14704-14718 (2011).
18. J. Xuan, M.K.H. Leung, D.Y.C. Leung, H. Wang, Applied Energy **90,** 80-86 (2012).
19. M.N. Nasharudin, S.K. Kamarudin, U.A. Hasran, M.S. Masdar, International Journal of Hydrogen Energy **39,** 1039-1055 (2014).
20. J. Xuan, D.Y.C. Leung, H. Wang, K.H. Leung, B. Wang, M. Ni, Applied Energy **104**, 400-407 (2013).
21. K.S. Salloum, J.R. Hayes, C.A. Friesen, J.D. Posner, Journal of Power Sources **180**, 243-252 (2008).
22. A.M. Zuria, A. Dector, F.M.C. Muniz, J.P. Esquivel, N. Sabate, J.L. Garcia, L.G. Arriaga, A.U.C. Ramirez, of Power Sources **269**, 783-788 (2014).
23. Z. Belkhiri, H.B. Moussa, D. Haddad, K. Oulmi, International Journal of Hydrogen Energy **40,** 13789-13798 (2015).
24. J.L. Cohen, D.A. Westly, A. Pechenik, H.D. Abruna, Journal of Power Sources **139,** 96-105 (2005).
25. E.R. Choban, L.J. Markoski, A. Wieckowski, P.J.A. Kenis, Journal of Power Sources **128** 54-60 (2004).
26. D.D. Ye, B. Zhang, X. Zhu, P.C. Sui, D. Djilali, Q. Liao, Journal of Power Sources **288**, 150-159 (2015).
27. J. Phirani, S. Basu, Sources **175,** 261-265 (2008).
28. D.M. Acosta, M.D.M. Acosta, L.A. Godinez, L.A. Contreras, S.M.D. Torres, J.L. Garcia, L.G. Arriaga, Journal of Power Sources **196**, 9270-9275 (2011).
29. T. Tsujiguchi, F. Matsuoka, Y. Hokari, Y. Osaka, A. Kodama, Electrochimica Acta, **197**, 32-38 (2016).
30. L. Li, G. Nikiforidis, K.H. Leung, W.A. Daoud, Applied Energy **177**, 729-739 (2016).